

TOI 694 b AND TIC 220568520 b: TWO LOW-MASS COMPANIONS NEAR THE HYDROGEN BURNING MASS LIMIT ORBITING SUN-LIKE STARS

ISMAEL MIRELES¹, AVI SHPORER¹, NOLAN GRIEVES², GEORGE ZHOU³, MAXIMILIAN N. GÜNTHER^{1,A}, RAFAEL BRAHM^{4,5}, CARL ZIEGLER⁶, KEIVAN G. STASSUN⁷, CHELSEA X. HUANG¹, LOUISE NIELSEN², LEONARDO A. DOS SANTOS², STÉPHANE UDRY², FRANOIS BOUCHY², MICHAEL IRELAND⁸, ALEXANDER WALLACE⁸, PAULA SARKIS⁹, THOMAS HENNING⁹, ANDRÉS JORDÁN^{4,5}, NICHOLAS LAW¹⁰, ANDREW W. MANN¹⁰, LEONARDO A. PAREDES¹¹, HODARI-SADIKI JAMES¹¹, WEI-CHUN JAO¹¹, TODD J. HENRY¹², R. PAUL BUTLER¹³, JOSEPH E. RODRIGUEZ¹⁴, LIANG YU¹, ERIN FLOWERS^{15,B}, GEORGE R. RICKER¹, DAVID W. LATHAM³, ROLAND VANDERSPEK¹, SARA SEAGER^{1,16,17}, JOSHUA N. WINN¹⁵, JON M. JENKINS¹⁸, GABOR FURESZ¹, KATHARINE HESSE¹⁹, ELISA V. QUINTANA²⁰, MARK E. ROSE¹⁸, JEFFREY C. SMITH^{18,21}, PETER TENENBAUM^{18,21}, MICHAEL VEZIE¹⁶, DANIEL A. YAHALOMI³, ZHUCHANG ZHAN¹⁶

Draft version July 14, 2020

ABSTRACT

We report the discovery of TOI 694 b and TIC 220568520 b, two low-mass stellar companions in eccentric orbits around metal-rich Sun-like stars, first detected by the Transiting Exoplanet Survey Satellite (*TESS*). TOI 694 b has an orbital period of 48.05131 ± 0.00019 days and eccentricity of 0.51946 ± 0.00081 , and we derive a mass of $89.0 \pm 5.3 M_{\text{Jup}}$ ($0.0849 \pm 0.0051 M_{\odot}$) and radius of $1.111 \pm 0.017 R_{\text{Jup}}$ ($0.1142 \pm 0.0017 R_{\odot}$). TIC 220568520 b has an orbital period of 18.55769 ± 0.00039 days and eccentricity of 0.0964 ± 0.0032 , and we derive a mass of $107.2 \pm 5.2 M_{\text{Jup}}$ ($0.1023 \pm 0.0050 M_{\odot}$) and radius of $1.248 \pm 0.018 R_{\text{Jup}}$ ($0.1282 \pm 0.0019 R_{\odot}$). Both binary companions lie close to and above the Hydrogen burning mass threshold that separates brown dwarfs and the lowest mass stars, with TOI 694 b being $2\text{-}\sigma$ above the canonical mass threshold of $0.075 M_{\odot}$. The relatively long periods of the systems mean that the magnetic fields of the low-mass companions are not expected to inhibit convection and inflate the radius, which according to one leading theory is common in similar objects residing in short-period tidally-synchronized binary systems. Indeed we do not find radius inflation for these two objects when compared to theoretical isochrones. These two new objects add to the short but growing list of low-mass stars with well-measured masses and radii, and highlight the potential of the *TESS* mission for detecting such rare objects orbiting bright stars.

Subject headings: Low mass stars, M dwarfs, Eclipsing binaries, stars: individual (TOI 694, TIC 55383975, TIC 220568520)

¹ Department of Physics and Kavli Institute for Astrophysics and Space Research, Massachusetts Institute of Technology, Cambridge, MA 02139, USA

² Observatoire astronomique de l'Université de Genève, 51 Chemin des Maillettes, 1290 Versoix, Switzerland

³ Harvard-Smithsonian Center for Astrophysics, 60 Garden Street, Cambridge, MA 02138, USA

⁴ Facultad de Ingeniería y Ciencias, Universidad Adolfo Ibáñez, Av. Diagonal las Torres 2640, Peñalolén, Santiago, Chile

⁵ Millennium Institute for Astrophysics, Chile

⁶ Dunlap Institute for Astronomy and Astrophysics, University of Toronto, 50 St. George Street, Toronto, Ontario M5S 3H4, Canada

⁷ Vanderbilt University, Department of Physics & Astronomy, 6301 Stevenson Center Lane, Nashville, TN 37235, USA

⁸ Research School of Astronomy and Astrophysics, Australian National University, Canberra, ACT 2611, Australia

⁹ Max-Planck-Institut für Astronomie, Königstuhl 17, 69117 Heidelberg, Germany

¹⁰ Department of Physics and Astronomy, The University of North Carolina at Chapel Hill, Chapel Hill, NC 27599-3255, USA

¹¹ Physics and Astronomy Department, Georgia State University, Atlanta, GA 30302, USA

¹² RECONS Institute, Chambersburg, PA, USA

¹³ Earth & Planets Laboratory, Carnegie Institution for Science, 5241 Broad Branch Road, NW, Washington, DC 20015, USA

¹⁴ Center for Astrophysics | Harvard & Smithsonian, 60 Garden St, Cambridge, MA 02138, USA

¹⁵ Department of Astrophysical Sciences, Princeton University, Princeton, NJ 08544, USA

¹⁶ Department of Earth, Atmospheric, and Planetary Sciences, Massachusetts Institute of Technology, Cambridge, MA 02139, USA

¹⁷ Department of Aeronautics and Astronautics, MIT, 77 Massachusetts Avenue, Cambridge, MA 02139, USA

¹⁸ NASA Ames Research Center, Moffett Field, CA 94035, USA

¹⁹ Department of Astronomy, Wesleyan University, Middletown, CT 06459, USA

²⁰ NASA Goddard Space Flight Center, 8800 Greenbelt Road, Greenbelt, MD 20771, USA

²¹ SETI Institute, Mountain View, CA 94043, USA

^A Juan Carlos Torres Fellow

^B NSF Graduate Research Fellow

1. INTRODUCTION

The stellar initial mass function (IMF) shows a maximum at or close to $0.1 M_{\odot}$, at the bottom of the main sequence (see e.g., Chabrier 2003; Bonnell et al. 2007; Andersen et al. 2008; Krumholz 2014, and references therein). That, combined with the increase in main sequence lifetime with decreasing stellar mass means that stars around $0.1 M_{\odot}$ are the most abundant stars in the galaxy. However, despite their abundance the precise measurement of their stellar properties, specifically radius and mass, is hindered by their low luminosity, leading to only a small number of objects at $\sim 0.1 M_{\odot}$ with precisely measured radius and mass.

Precise measurements of those properties are desirable, for example, when low-mass stars are found to host planets, since the precision of the measured planet parameters depends on the precision of the host star parameters. The latter is especially relevant to low-mass stars since their small radius and mass provides an opportunity to detect smaller planets orbiting them compared to larger, Sun-like stars (this is commonly known as the “M-dwarf opportunity”, see e.g. Gould et al. 2003; Nutzman & Charbonneau 2008).

One way to detect such low-mass stars whose mass and radius can be precisely measured is through wide-field photometric transit surveys. The signal searched for in those surveys scales quadratically with the radius of the transiting object, and the radius of the smallest stars is the same as that of gas giant planets, resulting in similar signals. This was already exemplified by several discoveries (e.g., Pont et al. 2005; Díaz et al. 2014; Zhou et al. 2014; Chaturvedi et al. 2016; von Boetticher et al. 2019).

A comparison between the sizes and masses of low-mass stars to theoretical predictions has shown that the measured stellar radii tend to be larger than expected (e.g. Ribas 2006; Torres et al. 2010; Kesseli et al. 2018) by about 5–10%. The leading hypothesis for the inflated stellar radius is strong magnetic fields that inhibit convection, leading to decreased heat flow and in turn increased radius (Chabrier et al. 2007). The magnetic fields are strengthened by the relatively fast stellar rotation resulting from spin-orbit tidal synchronization in short orbital period systems (Mazeh 2008). Given that these systems are detected through photometric transit surveys it is not surprising they tend to have short periods (shorter than ~ 10 days).

Here we present the discovery of two longer-period eclipsing binary systems with low-mass companions close to $0.1 M_{\odot}$ detected by the Transiting Exoplanet Survey Satellite (*TESS*) mission: TOI 694 b, with a period of 48.1 days, and TIC 220568520 b, with a period of 18.6 days. The long orbital periods mean that the companions are not expected to be tidally synchronized, so they are not expected to rotate rapidly and their magnetic fields are not expected to be strong enough to impact the stellar radius. We describe the *TESS* and ground-based observations in Section 2, and the data analysis in Section 3. We discuss our results in Section 4 and conclude with a summary in Section 5.

2. OBSERVATIONS

Basic photometric and astrometric information about the two targets studied here is given in Table 1.

2.1. *TESS* Photometry

TOI 694 (TIC 55383975; $V = 11.963$ mag) was observed by *TESS* Camera 4 during a total of 12 Sectors. It was observed in 2-minute cadence on Sector 1 (UT 2018 July 25 to UT 2018 August 22), Sectors 4 through 9 (UT 2018 October 18 to UT 2019 March 26), and Sectors 11 through 13 (UT 2019 April 22 to UT 2019 July 18). The target was within the field of view also in Sectors 2 and 3 (UT 2018 August 22 to UT 2018 October 18), but since it was not included in the pixel stamps observed with 2 minute exposures during those sectors we use the Full Frame Image (FFI) observations with a cadence of 30 minutes. *TESS* observations were interrupted between each of the 13.7 day long orbits of the satellite when data were downloaded to Earth. The 2-minute data were processed by the Science Processing Operations Center (SPOC; Jenkins et al. 2016) pipeline which produced two light curves per sector called Simple Aperture Photometry (SAP) and Presearch Data Conditioning Simple Aperture Photometry (PDCSAP; Smith et al. 2012; Stumpe et al. 2012; Stumpe et al. 2014) and identified 1.5% deep transit-like dips every 48.1 days. The FFIs were processed by the Quick Look Pipeline (QLP; Huang et al. in prep.). The *TESS* light curves are shown in Figures 1 and 2.

TIC 220568520 ($V = 12.039$ mag) was observed by *TESS* Camera 3 during Sectors 1 through 3, from UT 2018 July 25 to UT 2018 October 18. The target’s light curve was derived from the FFIs, with a 30 minute exposure time, by QLP where transits were identified with a high signal to noise ratio (SNR) every 18.2 days. The *TESS* light curves are shown in Figures 3 and 4. The decreased scatter in Figures 3 and 4 relative to Figures 1 and 2 is due to the longer integration time, which decreases the noise per exposure.

2.2. Spectroscopic follow-up

To characterize the stellar properties of the primary star and measure the mass of the transiting companion we obtained series of spectroscopic observations with the 1.5 m SMARTS/CHIRON, ANU 2.3 m/Echelle, Euler 1.2 m/CORALIE, and MPG/ESO 2.2 m/FEROS facilities. The radial velocity (RV) measurements are summarized in Table 2 and shown in Figures 5 and 6 for TOI 694 and TIC 220568520, respectively.

For both objects we obtained time series radial velocity with the 1.5 m SMARTS/CHIRON facility (Tokovinin et al. 2013), located at Cerro Tololo Inter-American Observatory (CTIO), Chile. The spectra were obtained with CHIRON in the fiber mode, with a spectral resolving power of $R \sim 25,000$ over the wavelength region of 4100 Å to 8700 Å. These observations were used to constrain the systems’ RV orbit. Fourteen CHIRON spectra were obtained for TOI 694 from UT 2019 October 7 to UT 2020 February 17, and ten spectra were obtained for TIC 220568520 from 2019 August 31 to 2019 October 7. RVs were measured from each spectrum by modeling their rotational line profiles, derived via a least-square deconvolution (Donati et al. 1997) of the observed spectrum against a non-rotating synthetic template generated with the ATLAS-9 model atmospheres (Castelli &

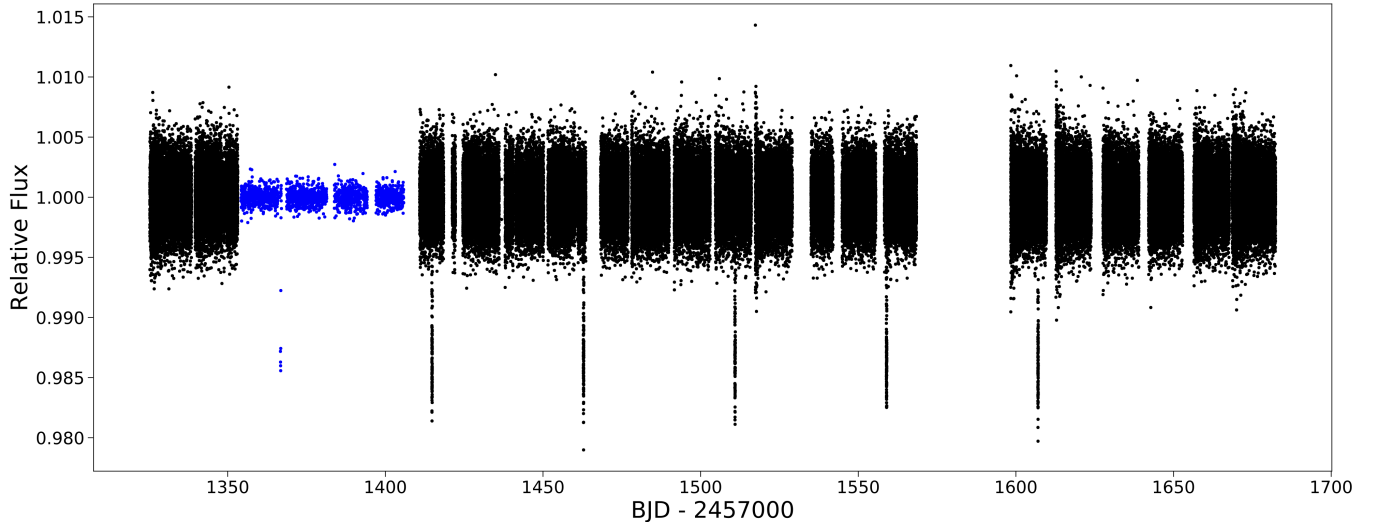


FIG. 1.— The detrended SPOC 2-minute (black) and QLP 30-minute cadence (blue) *TESS* light curve of TOI 694. Six transits are clearly seen, 5 of which were observed with 2-minute cadences.

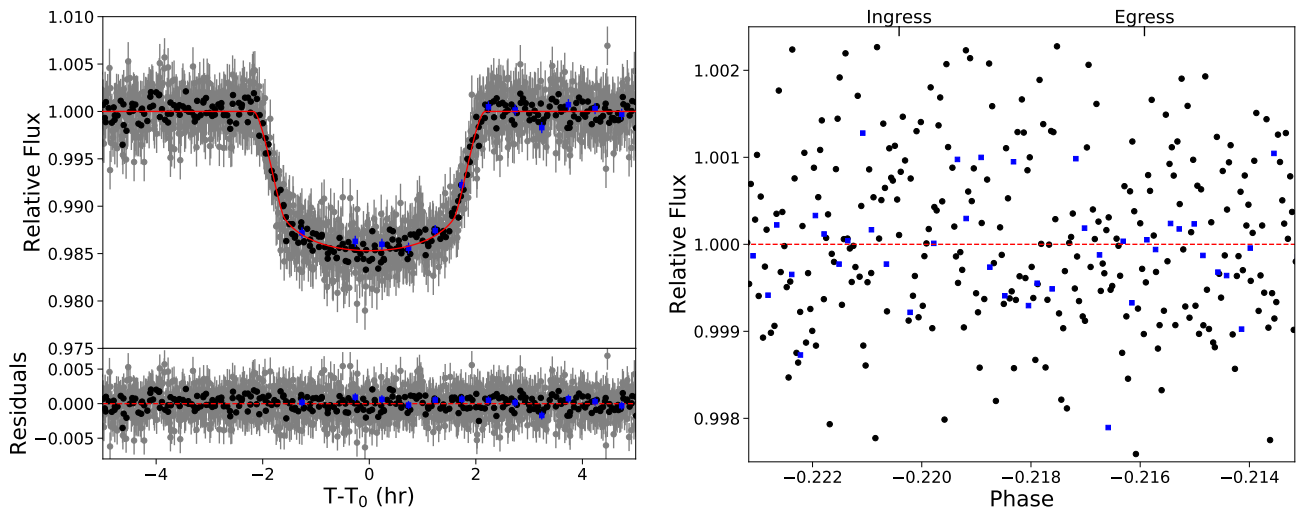


FIG. 2.— Zoom-in view of the phased *TESS* 2-minute cadence (grey), binned 2-minute cadence (black), and 30-minute cadence (blue) light curve of the TOI 694 transit (left panel) and secondary eclipse (right panel). In the left panel, the red line is the fitted transit model, and the residuals (data - model) are shown at the bottom. In the right panel, the dashed red line is the median relative flux value out of transit. The error bars are not shown in order to improve visibility. The ingress and egress points are denoted at the top of the figure.

Hubrig 2004). The derived RVs are listed in Table 2. In addition, for each target a single CHIRON spectrum was observed in the slicer mode, with a resolving power of $R \sim 80,000$, to be used for spectral characterization of the primary star, described in Section 3.1.

For TIC 220568520 we measured RVs with the Australian National University (ANU) 2.3m/Echelle spectrograph at Siding Spring Observatory (New South Wales, Australia) prior to obtaining the CHIRON spectra. The ANU 2.3m/Echelle is a slit-fed medium resolution spectrograph on the ANU 2.3m telescope, located at Siding Spring Observatory, Australia. The spectrograph has a spectral resolving power of $\lambda/\Delta\lambda \equiv R \sim 23,000$ over the wavelength range of 3900 Å to 6700 Å. A total of eleven spectra were obtained for TIC 220568520 with the ANU 2.3m from UT 2019 January 17 to UT 2019 March 4th, at an average signal-to-noise ratio of ~ 50

per resolution element over the Mg b Triplet wavelength region for each observation. The spectra were reduced and extracted based on the procedure described in Zhou et al. (2014), and are listed in Table 2.

We obtained nine observations of TOI-694 with the high resolution spectrograph CORALIE on the Swiss 1.2 m Euler telescope at La Silla Observatory, Chile (Queloz et al. 2001) between UT 2019 October 17 and UT 2020 January 7. CORALIE has a resolution of $R \sim 60,000$ and is fed by two fibers: a 2 arcsec on-sky science fiber encompassing the star and another fiber that can either connect to a Fabry-Pérot etalon for simultaneous wavelength calibration or on-sky for background subtraction of sky flux. We observed TOI-694 in the simultaneous Fabry-Pérot wavelength calibration mode using an exposure time of 1800 seconds. The spectra were reduced with the CORALIE standard reduction pipeline and RVs

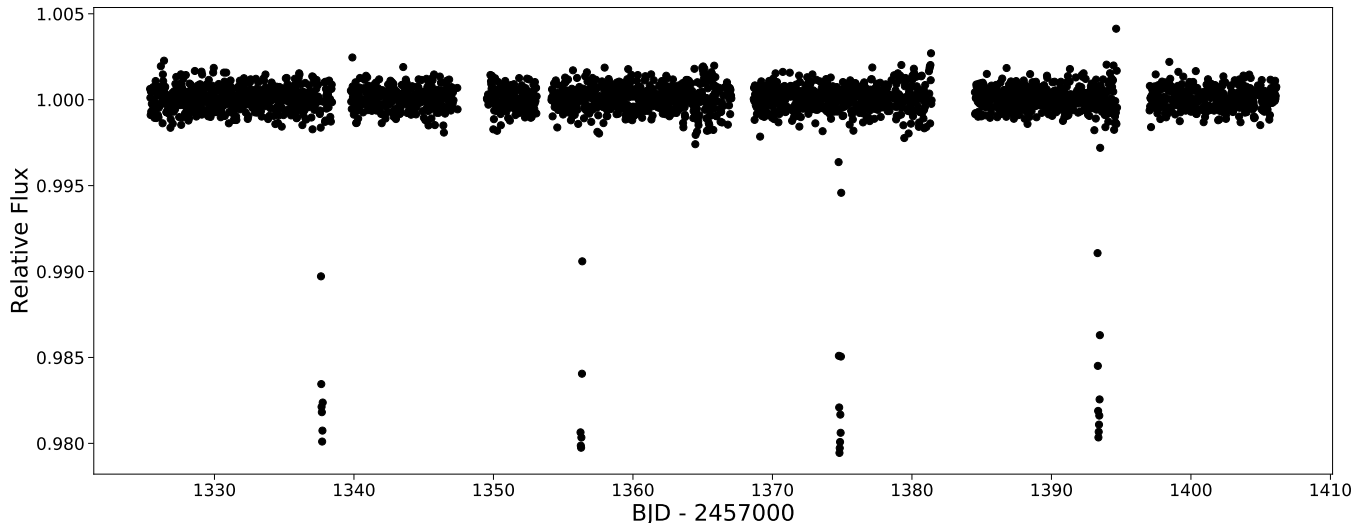


FIG. 3.— 30-minute cadence *TESS* light curve of TIC 220568520 with 4 clear transit events.

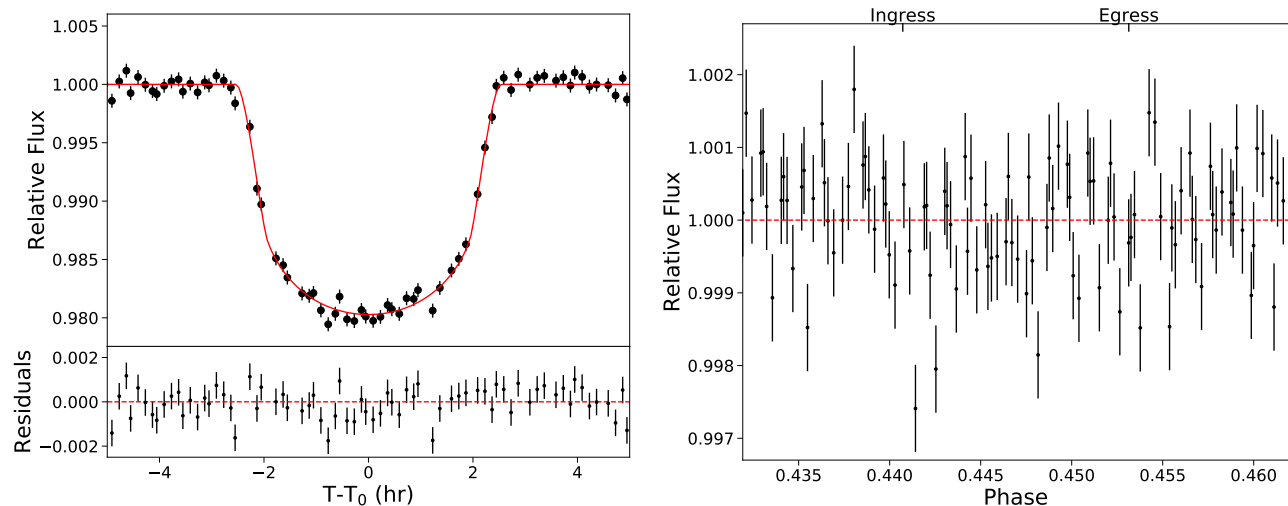


FIG. 4.— Zoom-in of the phased *TESS* light curve of TIC 220568520, centered on mid-transit (left) and the secondary eclipse (right). In the left panel, the red line is the fitted transit model, and the residual (data - model) are shown at the bottom. In the right panel, the dashed red line is the median relative flux value out of transit.

were computed for each epoch by cross-correlating with a binary G2 mask (Pepe et al. 2002).

TOI-694 was observed also with the Fiber-fed, Extended Range, Echelle Spectrograph (FEROS; Kaufer et al. 1999), mounted on the MPG/ESO 2.2 m telescope at La Silla, Chile. observations were done by the WINE collaboration, which is focused on the systematic characterization of warm giant planets with *TESS* (Brahm et al. 2019; Jordán et al. 2020). Four spectra of TOI-694 were obtained between UT 2019 February 28 and UT 2019 March 17 with an exposure time of 900 sec and a SNR ranging from 53 to 76. Observations were performed with the simultaneous calibration technique, where a comparison fiber is used to trace the instrumental variations during the science exposure by registering the spectrum of a ThAr lamp. FEROS data were reduced and processed with the CERES pipeline (Brahm et al. 2017) which uses the optimal extraction routines presented by Marsh (1989) and delivers precise RVs and bi-

sector span measurements, which are presented in Table 2.

2.3. High Angular Resolution Imaging with SOAR HRCam

We used high angular resolution imaging in order to look for stars close to the targets' position, within an angular separation of 1–2'', which cannot be identified with regular seeing-limited imaging. If they exist, the small separation might prevent them from being detected by Gaia and included in the TIC (Stassun et al. 2018), leading to an inaccurate estimate of the extent by which light from the target is blended with light from nearby stars, leading in turn to a biased estimate of the intrinsic transit depth. It is also possible that nearby stars are the source of the variability seen in *TESS* data.

We observed both targets with the high resolution camera (HRCam, Tokovinin 2018) mounted on the southern astrophysical research (SOAR) 4.1 m telescope, in Cerro

TABLE 1
TARGET INFORMATION

| Parameter | TOI 694 | TIC 220568520 | Source |
|-------------------------------------|--------------------|--------------------|------------------------|
| TIC | 55383975 | 220568520 | TIC V8 ^a |
| R.A. | 05:09:32.06 | 03:05:08.58 | Gaia DR2 ^b |
| Dec. | -64:01:33.9 | -62:51:24.56 | Gaia DR2 ^b |
| μ_{ra} (mas yr ⁻¹) | 6.468 ± 0.044 | 16.381 ± 0.038 | Gaia DR2 ^b |
| μ_{dec} (mas yr ⁻¹) | 25.987 ± 0.054 | 14.579 ± 0.036 | Gaia DR2 ^b |
| Parallax (mas) | 4.438 ± 0.025 | 4.087 ± 0.021 | Gaia DR2 ^b |
| Epoch | 2015.5 | 2015.5 | Gaia DR2 ^b |
| B (mag) | 12.761 ± 0.015 | 13.326 ± 0.045 | AAVSO DR9 ^c |
| V (mag) | 11.963 ± 0.069 | 12.039 ± 0.05 | AAVSO DR9 ^c |
| $Gaia$ (mag) | 11.7733 ± 0.00025 | 11.83746 ± 0.00023 | Gaia DR2 ^b |
| B_P (mag) | 12.2037 ± 0.0017 | 12.82419 ± 0.00075 | Gaia DR2 ^b |
| R_P (mag) | 11.21367 ± 0.00092 | 11.29765 ± 0.00055 | Gaia DR2 ^b |
| $TESS$ (mag) | 11.2595 ± 0.006 | 11.3458 ± 0.006 | TIC V8 ^a |
| J (mag) | 10.616 ± 0.024 | 10.687 ± 0.026 | 2MASS ^d |
| H (mag) | 10.207 ± 0.021 | 10.333 ± 0.022 | 2MASS ^d |
| K_S (mag) | 10.108 ± 0.019 | 10.270 ± 0.023 | 2MASS ^d |

^a Stassun et al. (2018).

^b Gaia Collaboration et al. (2018).

^c Henden et al. (2016).

^d Cutri et al. (2003).

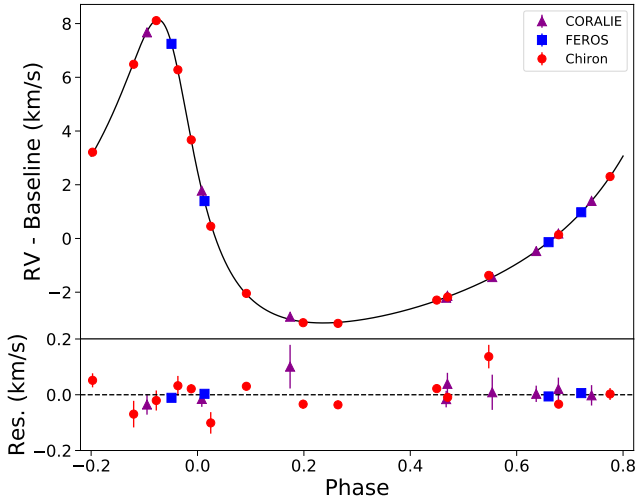


FIG. 5.— Radial velocity curve of TOI 694 phase folded to the orbital period of the companion. The different colors and markers correspond to the different instruments used to obtain the data, and the black line denotes the best-fit model. The residuals for each instrument are shown in the bottom panel.

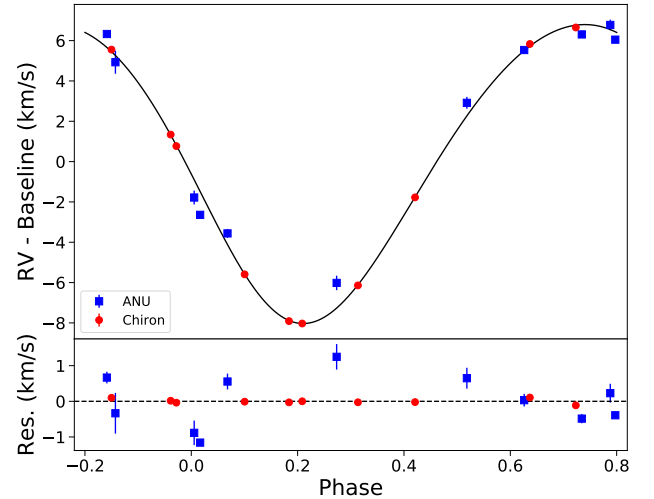


FIG. 6.— Radial velocity curve of TIC 220568520 phase folded to the orbital period of the companion. The different colors and markers correspond to the different instruments used to obtain the data, and the black line denotes the best-fit model. The residuals for each instrument are shown in the bottom panel.

Pachón, Chile. HRCam uses the speckle interferometry technique in a visible bandpass similar to that of *TESS*. A detailed description of HRCam observations of *TESS* targets is available in Ziegler et al. (2020). We observed TOI 694 on UT 2019 July 14 and TIC 220568520 on UT 2019 November 9. For both targets we detected no nearby sources down to $\Delta\text{mag} \approx 4.5$ mag at $0.3''$ and $\Delta\text{mag} \approx 5.0$ at $1.0''$. The $5\text{-}\sigma$ SOAR/HRCam detection sensitivity and the speckle auto-correlation function are plotted in Figures 7 and 8.

3. DATA ANALYSIS

3.1. Primary Star Parameters

3.1.1. MESA Isochrones and Stellar Tracks Analysis

For the primary star in each system we derived initial values of the spectral parameters, T_{eff} , $\log g$, and $V \sin(I)$, by matching each CHIRON spectrum against a library of $\sim 10,000$ observed spectra classified by the Stellar Parameter Classification routine (Buchhave et al. 2012).

We then used the spectroscopic parameters along with the Gaia DR2 parallax and magnitudes (G , B_P , R_P), 2MASS magnitudes (J , H , K_S), and AAVSO magnitudes (B , V) to perform an isochrone fit in order to further constrain the spectroscopic parameters and derive physical parameters for the primary stars. The spectroscopic parameters, parallax, and magnitudes are used as priors to determine the goodness of fit. We use the *isochrone* package (Morton 2015) to generate the isochrone models used to sample the stellar parameters and find the best-fit pa-

TABLE 2
RADIAL VELOCITIES

| Time BJD | RV ^a km s ⁻¹ | Error km s ⁻¹ | Instrument |
|----------------------------|---------------------------------------|-----------------------------|-------------------|
| TOI 694 ^b | | | |
| 2458542.63751 | 21.4803 | 0.0076 | FEROS |
| 2458545.58904 | 22.5943 | 0.0071 | FEROS |
| 2458556.62596 | 28.8646 | 0.0095 | FEROS |
| 2458559.60797 | 23.0099 | 0.0077 | FEROS |
| 2458763.86992 | 16.2069 | 0.0149 | CHIRON |
| 2458772.79219 | 17.0740 | 0.0104 | CHIRON |
| 2458773.77718 | 17.1886 | 0.0145 | CHIRON |
| 2458783.80427 | 19.5069 | 0.0068 | CHIRON |
| 2458789.75347 | 22.5803 | 0.0252 | CHIRON |
| 2458798.66760 | 23.0389 | 0.0159 | CHIRON |
| 2458803.64710 | 17.3233 | 0.0147 | CHIRON |
| 2458808.77574 | 16.2327 | 0.0156 | CHIRON |
| 2458873.59450 | 17.9937 | 0.0422 | CHIRON |
| 2458884.55191 | 21.6734 | 0.0214 | CHIRON |
| 2458889.56772 | 25.8525 | 0.0477 | CHIRON |
| 2458891.61208 | 27.4781 | 0.0359 | CHIRON |
| 2458893.56327 | 25.6463 | 0.0351 | CHIRON |
| 2458896.53063 | 19.8216 | 0.0386 | CHIRON |
| 2458773.75679 | 19.5107 | 0.0396 | CORALIE |
| 2458777.80659 | 20.2075 | 0.0631 | CORALIE |
| 2458781.77898 | 21.1769 | 0.0293 | CORALIE |
| 2458783.78105 | 21.8304 | 0.0406 | CORALIE |
| 2458786.77769 | 23.0417 | 0.0366 | CORALIE |
| 2458821.69504 | 19.4387 | 0.0295 | CORALIE |
| 2458842.72232 | 29.3174 | 0.0362 | CORALIE |
| 2458847.67201 | 23.4254 | 0.0283 | CORALIE |
| 2458855.64763 | 18.7321 | 0.0783 | CORALIE |
| TIC 220568520 ^c | | | |
| 2458500.97894 | 30.5575 | 0.0318 | ANU 2.3 m/Echelle |
| 2458502.09007 | 29.4386 | 0.5716 | ANU 2.3 m/Echelle |
| 2458505.04661 | 21.8699 | 0.0795 | ANU 2.3 m/Echelle |
| 2458506.00173 | 20.9493 | 0.2224 | ANU 2.3 m/Echelle |
| 2458532.91371 | 27.4253 | 0.2931 | ANU 2.3 m/Echelle |
| 2458534.91425 | 30.0442 | 0.1773 | ANU 2.3 m/Echelle |
| 2458536.92492 | 30.8171 | 0.1309 | ANU 2.3 m/Echelle |
| 2458537.91918 | 31.2864 | 0.2634 | ANU 2.3 m/Echelle |
| 2458538.90685 | 30.8376 | 0.1639 | ANU 2.3 m/Echelle |
| 2458541.95366 | 22.7282 | 0.3439 | ANU 2.3 m/Echelle |
| 2458546.92590 | 18.4931 | 0.3579 | ANU 2.3 m/Echelle |
| 2458726.90477 | 24.0542 | 0.0239 | CHIRON |
| 2458730.83770 | 15.3734 | 0.0217 | CHIRON |
| 2458740.84783 | 29.9363 | 0.0211 | CHIRON |
| 2458747.84631 | 17.6927 | 0.0115 | CHIRON |
| 2458749.85537 | 15.2544 | 0.0140 | CHIRON |
| 2458751.80097 | 17.1443 | 0.0172 | CHIRON |
| 2458753.79406 | 21.5104 | 0.0119 | CHIRON |
| 2458757.80128 | 29.1168 | 0.0187 | CHIRON |
| 2458761.75638 | 28.8378 | 0.0263 | CHIRON |
| 2458763.82222 | 24.6238 | 0.0131 | CHIRON |

^a All radial velocities are barycentric.

^b The Gaia DR2 RV is 20.70 ± 2.22 km s⁻¹ (Lindgren et al. 2018).

^c The Gaia DR2 RV is 28.09 ± 1.79 km s⁻¹ (Lindgren et al. 2018).

rameters by using an MCMC routine. The routine consists of 40 independent walkers each taking 25000 steps, of which the first 2000 are discarded as burn-in.

The fitted spectroscopic parameters and derived physical parameters for the primary stars in each of the two systems studied here are reported in Table 3. Both pri-

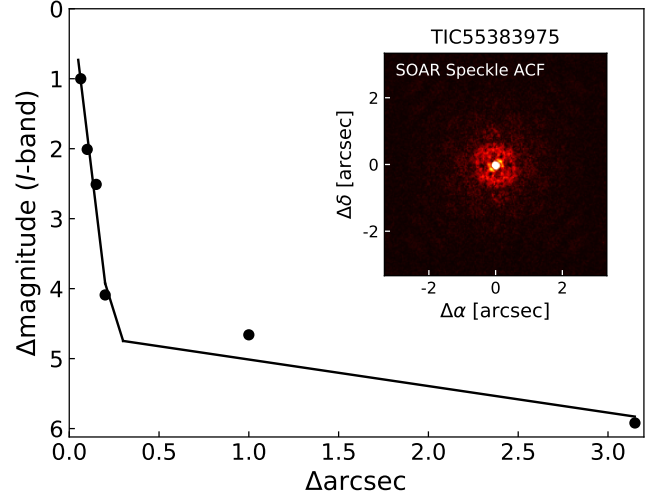


FIG. 7.— Contrast curves showing the 5- σ detection sensitivity and speckle auto-correlation functions obtained in I-band using SOAR/HRCam for TOI 694 (TIC 55383975).

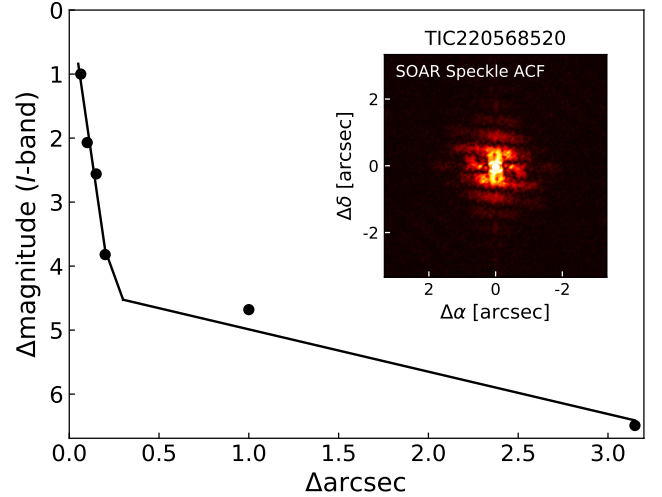


FIG. 8.— Contrast curves showing the 5- σ detection sensitivity and speckle auto-correlation functions obtained in I-band using SOAR/HRCam for TIC 220568520.

mary stars are similar to each other, and similar to the Sun (within 1–2 σ) albeit with higher metallicities.

3.1.2. Spectral Energy Distribution Analysis

For both TOI 694 and TIC 220568520 we performed an analysis of the broadband spectral energy distribution (SED) together with the *Gaia* DR2 parallax in order to determine an empirical measurement of the stellar radius, following the procedures described in Stassun & Torres (2016); Stassun et al. (2017, 2018). We pulled the *BVgr* magnitudes from APASS, the *JHK_S* magnitudes from *2MASS*, the W1–W4 magnitudes from *WISE*, and the *GG_{BP}GRP* magnitudes from *Gaia*. We also considered the *GALEX* NUV flux for evidence of chromospheric activity. Together, the available photometry spans the full stellar SED over the wavelength range of 0.2–22 μ m (see Figure 9).

We performed a fit using Kurucz stellar atmosphere models, with the priors on effective temperature (T_{eff}), surface gravity ($\log g$), and metallicity ($[\text{Fe}/\text{H}]$) from

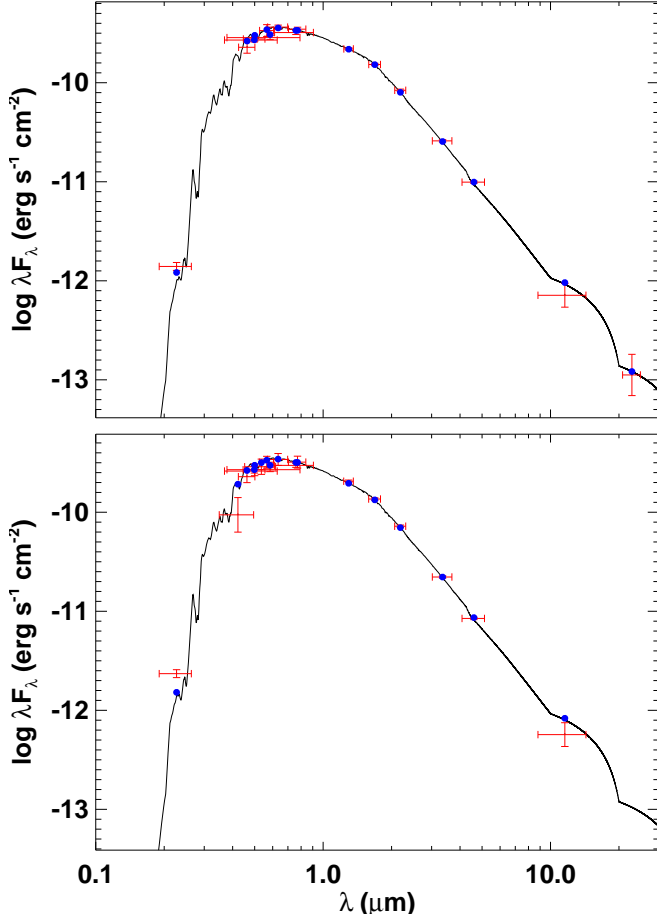


FIG. 9.— Spectral energy distribution (SED) for TOI 694 (top) and TIC 220568520 (bottom). Red symbols represent the observed photometric measurements, where the horizontal bars represent the effective width of the passband. Blue symbols are the model fluxes from the best-fit Kurucz atmosphere model (black).

the analysis of the CHIRON spectra. The remaining free parameter is the extinction (A_V), which we limited to the maximum permitted for the star’s line of sight from the Schlegel et al. (1998) dust maps. The resulting fits, plotted in Figure 9, have a reduced χ^2 of 1.3 and 2.1, and $A_V = 0.12 \pm 0.02$ and 0.06 ± 0.02 , for TOI 694 and TIC 220568520, respectively. Integrating the model SED gives the bolometric flux at Earth of $F_{\text{bol}} = 5.199 \pm 0.060 \times 10^{-10} \text{ erg s}^{-1} \text{ cm}^{-2}$ and $4.77 \pm 0.11 \times 10^{-10} \text{ erg s}^{-1} \text{ cm}^{-2}$, respectively. Taking the F_{bol} and T_{eff} together with the *Gaia* parallax, adjusted by $+0.08 \text{ mas}$ to account for the systematic offset reported by Stassun & Torres (2018), gives the stellar radii as $R_s = 0.992 \pm 0.037 R_\odot$ and $0.992 \pm 0.038 R_\odot$, respectively.

3.1.3. Stellar Mass via Radius and Surface Gravity

The empirical stellar radii determined above affords an opportunity to estimate the stellar masses empirically as well, via the spectroscopically determined surface gravity ($\log g = 4.45 \pm 0.10$ and 4.34 ± 0.10 , respectively). For TOI 694 and TIC 220568520 we obtain $M_s = 1.01 \pm 0.13 M_\odot$ and $0.79 \pm 0.19 M_\odot$, respectively. These are similar to the values estimated via the eclipsing-binary based relations of Torres et al. (2010), which give $M_s = 1.00 \pm 0.06 M_\odot$ and $1.09 \pm 0.07 M_\odot$,

respectively. For TOI 694, these values are nearly identical. For TIC 220568520, they differ by less than 2σ .

3.1.4. Stellar Age via Gyrochronology

We estimate each star’s age from its rotational period, P_{rot} , which we calculate from the spectroscopic $V \sin(I)$ together with the empirically determined radius above, assuming $I = 90^\circ$. For TOI 694 and TIC 220568520 we obtain $P_{\text{rot}} \approx 24.1 \pm 5.6 \text{ d}$ and $15.5 \pm 2.3 \text{ d}$, respectively. From the rotation-activity-age relations of Mamajek & Hillenbrand (2008), we obtain from the P_{rot} and the stellar $B - V$ colors ages of $\tau = 3.8 \pm 0.4 \text{ Gyr}$ and $2.3 \pm 0.3 \text{ Gyr}$, respectively.

3.2. Simultaneous Transit and RV Fit

In order to derive the orbital parameters and companion’s radius and mass, we performed model fitting using ALLESFITTER²⁴ (Günther, & Daylan 2019; Günther & Daylan 2020), enabling a joint analysis of the *TESS* transit light curve and the RV orbit. ALLESFITTER is publicly available, and provides an environment to analyze light curves and RVs of binary star and star-planet systems. It is based on various public packages including ELLC for light curve and RV modeling (Maxted 2016) and EMCEE for Markov Chain Monte Carlo sampling (Foreman-Mackey et al. 2013).

We fit the following parameters:

- quadratic stellar limb-darkening parameters q_1 and q_2 , using the transformation from Kipping (2013), with Gaussian priors centered on values derived from Claret (2017). We chose the Gaussian prior width (1σ) to be 0.1, which reflects the uncertainties on the host stars parameters.
- radius ratio, R_2/R_1 , where 1 denotes the primary star and 2 the secondary, with uniform prior from 0 to 1,
- sum of radii divided by the orbital semi-major axis, $(R_1 + R_2)/a$, with uniform prior from 0 to 1,
- cosine of the orbital inclination, $\cos i$, with uniform prior from 0 to 1,
- orbital period, P with uniform prior from 0 to 10^{12} days,
- Primary eclipse epoch, T_0 , with uniform prior from 0 to 10^{12} days,
- RV semi-amplitude, K , with uniform prior from 0 to 50 km s^{-1} ,
- eccentricity parameters $\sqrt{e \cos \omega}$ and $\sqrt{e \sin \omega}$, each with uniform prior from -1 to 1, where e is the orbital eccentricity and ω the argument of periastron,
- RV zero point, γ_c , for each of the RV data sets,
- RV jitter terms, σ_c , for each of the RV data sets,
- white noise scaling term for the *TESS* data, $\sigma_{c,TESS}$.

Initial guesses for the values of q_1 and q_2 were obtained by matching the spectroscopic parameters of each primary star to the closest values of the coefficients u_1 and

²⁴ <https://github.com/MNGuenter/allesfitter>

u_2 of the quadratic limb darkening law listed in Claret (2017), and transforming them to the corresponding values of q_1 and q_2 . Initial guesses for R_2/R_1 , $(R_1 + R_2)/a$, $\cos i$, P , and T_0 were obtained using values provided by the SPOC Data Validation Report for TOI 694 (Li et al. 2019) and QLP Data Validation Report for TIC 220568520. Initial guesses for K and the 4 γ_c terms were obtained by visually inspecting each data set. We used an MCMC algorithm to explore the parameter space and determine the best-fit parameters. We initialized the MCMC with 100 walkers, performing 2 preliminary runs of 1000 steps per walker to obtain higher-likelihood initial guesses for the nominal run of 15000 steps per walker. We then discarded the first 2000 steps for each chain as burn-in phase before thinning the chains by a factor of 10 and calculating the final posterior distributions. The values and errors of the fitted and derived parameters listed in Table 3 are defined as the median values and 68% confidence intervals of the posterior distributions, respectively. The best-fit transit model light curve and radial velocity model curve for TOI 694 are shown in Figures 2 and 5, respectively. For TIC 220568520, they are shown in Figures 4 and 6.

4. DISCUSSION

From the simultaneous fits of the *TESS* transit photometry and RV data, we derive TOI 694 b mass and radius to be $89.0 \pm 5.3 M_{\text{Jup}}$ ($0.0849 \pm 0.0051 M_{\odot}$) and $1.111 \pm 0.017 R_{\text{Jup}}$ ($0.1142 \pm 0.0017 R_{\odot}$), respectively, and TIC 220568520 b mass and radius to be $107.2 \pm 5.2 M_{\text{Jup}}$ ($0.1023 \pm 0.0050 M_{\odot}$) and $1.248 \pm 0.018 R_{\text{Jup}}$ ($0.1282 \pm 0.0019 R_{\odot}$), respectively. We note that mass uncertainties are dominated by the primary star mass uncertainties and not the orbital parameters uncertainties.

The two binary companions measured here are among the smallest stars with a measured radius and mass. To show them in the context of similar objects we plot in Figure 10 the radius-mass diagram spanning brown dwarfs and small stars, with a mass range of $0.01 - 0.21 M_{\odot}$. We mark on that diagram the new objects studied here (in red), and objects within that mass range that have a measured radius reported in the literature which we list in Table 4²⁵, with the exception of the inflated brown dwarf RIK 72 b (David et al. 2019).

We also plot in the radius-mass diagram the theoretical isochrones for solar metallicity at ages of 1, 5, and 10 Gyr taken from Baraffe et al. (2003, 2015), and the MESA isochrones and stellar tracks (MIST²⁶; Dotter 2016; Paxton et al. 2011) at 5 Gyr with solar metallicity and metallicity of $[\text{Fe}/\text{H}] = 0.25$. The latter is close to the metallicity we measure for the primary star in TIC 220568520 which we assume is also the metallicity of the secondary.

The position in the radius-mass diagram of TOI 694 studied here is consistent with the 8 Gyr and $[\text{Fe}/\text{H}] = 0.30$ isochrone from Saumon & Marley (2008). In con-

trast, the position of TIC 220568520 is slightly *below* the MIST relation for $[\text{Fe}/\text{H}] = 0.25$, with a distance in radius of about 5%. This small inconsistency is in the opposite direction of the inflated radius identified for stars of similar mass (e.g., Ribas 2006; Torres et al. 2010; Burrows et al. 2011; Kesseli et al. 2018) and believed to be the result of enhanced magnetic fields in rapidly rotating stars (e.g., Chabrier et al. 2007). However, the recent work of Han et al. (2019) and von Boetticher et al. (2019) showed that the radii of many low-mass fully convective stars are consistent with theoretical expectations without invoking enhanced magnetic fields.

Fast rotation, which leads to enhanced magnetic fields, can result from spin-orbit tidal synchronization of short period systems (Mazeh 2008). The two systems studied here have relatively long orbital periods, of 18.6 days (TIC 220568520) and 48.1 days (TOI 694), longer than 95% (TOI 694) and 87% (TIC 220568520) of the systems listed in Table 4. Therefore these systems are not expected to have reached tidal synchronization. Even if the low-mass binary companions have reached pseudo-synchronization (Hut 1981; Zimmerman et al. 2017), the rotation periods would be longer than the typical few days orbital periods of most of the systems in Table 4. Therefore, whether or not enhanced magnetic fields affect the radius of low-mass stars, it is not likely that they affect the radius of the two low-mass stars studied here.

Both systems studied here have a non-circular orbit, with well-measured orbital eccentricity. That is expected given their relatively long orbital periods, leading to a predicted orbital circularization time scale on the order of $10^{14} - 10^{15}$ years (Hilditch 2001). We show in Figure 11 the orbital eccentricity as a function of scaled semi-major axis and orbital period for all of the systems with brown dwarfs and low-mass stellar secondaries listed in Table 4. The figure shows TIC 220568520 with an eccentricity at the lower end of the eccentricity range of systems with similar orbital periods, and TOI 694 with an eccentricity close to the upper end of that of systems at similar orbital periods.

Tidal alignment for well separated binaries occurs on a similar timescale as tidal synchronization (Hut 1981). For the two systems studied here, the synchronization timescales are on the order of 10^{12} years, meaning that these systems are not expected to be aligned due to tidal alignment mechanisms, although, they may have formed in aligned configurations. Therefore, measuring the primary star’s obliquity, through the Rossiter-McLaughlin (RM) effect (e.g., Albrecht et al. 2007; Gaudi & Winn 2007; Triaud 2018), can probe their formation process (e.g., Pringle 1989; Bonnell et al. 1992; Bonnell 1994; Fabrycky & Tremaine 2007). The predicted semi-amplitudes of the RM RV signal are 17 m s^{-1} and 35 m s^{-1} for TOI 694 and TIC 220568520, respectively (Derived using Eq. 1 of Triaud 2018).

The well-measured orbits and transits allow us to calculate the expected phase and duration of the secondary eclipses, where the low-mass star moves behind the primary star. A detection of a secondary eclipse and a measurement of its depth can constrain the temperature of the low-mass object, leading to a more complete characterization. The phase folded light curves of TOI 694 and TIC 220568520 during secondary eclipse phase are plot-

²⁵ The list given in Table 4 is the result of our efforts to compile all objects reported in the literature within the mass range of $0.01 - 0.21 M_{\odot}$ whose radius is also measured. While we recognize the possibility that a few objects may have unintentionally been omitted from such a compilation, such omission is highly unlikely to change the characteristics of the population of these objects, as presented in Figures 10 and 11 and discussed in the text.

²⁶ <http://waps.cfa.harvard.edu/MIST/>

TABLE 3
FITTED AND DERIVED PARAMETERS

| Parameter | TOI 694 | | TIC 220568520 | |
|---|------------|----------------------|---------------|----------------------|
| | Value | Error | Value | Error |
| <i>Host star Parameters</i> | | | | |
| M_1 (M_\odot) | 0.967 | +0.047 -0.040 | 1.030 | +0.043 -0.042 |
| R_1 (R_\odot) | 0.998 | +0.010 -0.012 | 1.007 | +0.010 -0.009 |
| ρ_1^a (g cm^{-3}) | 1.51 | +0.15 -0.13 | 1.445 | +0.064 -0.074 |
| L_1 (L_\odot) | 0.819 | +0.047 -0.044 | 0.890 | +0.047 -0.044 |
| T_{eff} (K) | 5496 | +87 -81 | 5589 | 81 |
| [Fe/H] | 0.21 | 0.08 | 0.26 | 0.07 |
| $\log g$ | 4.425 | +0.028 -0.025 | 4.445 | +0.023 -0.025 |
| Age (Gyr) | 7.33 | +2.92 -3.02 | 4.09 | +2.60 -2.28 |
| $V \sin(I)$ (km s^{-1}) | 2.18 | 0.5 | 3.4 | 0.5 |
| <i>Fitted parameters</i> | | | | |
| q_1, TESS | 0.345 | +0.078 -0.070 | 0.418 | +0.080 -0.074 |
| q_2, TESS | 0.308 | +0.084 -0.079 | 0.374 | 0.071 |
| R_2/R_1 | 0.1145 | +0.0012 -0.0013 | 0.1274 | +0.0014 -0.0013 |
| $(R_1 + R_2)/a$ | 0.01960 | 0.00064 | 0.03791 | +0.00070 -0.00056 |
| $\cos i$ | 0.0152 | +0.0020 -0.0023 | 0.0075 | +0.0030 -0.0040 |
| T_0 (BJD - 2,457,000) | 1366.77176 | 0.00064 | 1337.72060 | 0.00082 |
| P (d) | 48.05131 | 0.00019 | 18.55769 | 0.00039 |
| K (km s^{-1}) | 5.645 | 0.011 | 7.428 | 0.035 |
| $\sqrt{e} \cos \omega$ | 0.61438 | +0.00072 -0.00078 | -0.2709 | 0.0080 |
| $\sqrt{e} \sin \omega$ | 0.3768 | +0.0016 -0.0015 | 0.151 | 0.016 |
| $\gamma_{c, \text{ANU}}$ (km s^{-1}) | - | - | 24.50 | 0.22 |
| $\gamma_{c, \text{CHIRON}}$ (km s^{-1}) | 19.368 | 0.013 | 23.285 | 0.028 |
| $\gamma_{c, \text{FEROS}}$ (km s^{-1}) | 21.6187 | 0.0062 | - | - |
| $\gamma_{c, \text{CORALIE}}$ (km s^{-1}) | 21.645 | 0.012 | - | - |
| $\ln \sigma_{c, \text{ANU}}$ [km s^{-1}] | - | - | -0.37 | +0.21 -0.23 |
| $\ln \sigma_{c, \text{CHIRON}}$ [km s^{-1}] | -3.21 | 0.34 | -2.56 | +0.36 -0.30 |
| $\ln \sigma_{c, \text{FEROS}}$ [km s^{-1}] | -12.7 | 6.9 | - | - |
| $\ln \sigma_{c, \text{CORALIE}}$ [km s^{-1}] | -13.5 | 6.5 | - | - |
| $\ln \sigma_{c, \text{TESS}_{SC}}$ ^b | -6.242 | 0.012 | - | - |
| $\ln \sigma_{c, \text{TESS}_{LC}}$ ^c | -7.21 | +0.20 -0.17 | -7.313 | 0.055 |
| <i>Derived Parameters</i> | | | | |
| i ($^\circ$) | 89.13 | +0.13 -0.11 | 89.57 | +0.23 -0.17 |
| a (AU) | 0.2638 | +0.0092 -0.0086 | 0.1391 | +0.0025 -0.0027 |
| b^d | 0.497 | +0.048 -0.060 | 0.211 | +0.081 -0.11 |
| T_{tot}^e (h) | 4.328 | +0.037 -0.035 | 5.018 | 0.035 |
| T_{full}^f (h) | 3.179 | 0.068 | 3.834 | +0.050 -0.058 |
| e | 0.51946 | 0.00081 | 0.0964 | +0.0034 -0.0030 |
| ω (deg) | 31.52 | +0.13 -0.12 | 150.9 | 3.2 |
| R_2 (R_{Jup}) | 1.111 | 0.017 | 1.248 | 0.018 |
| M_2 (M_{Jup}) | 89.0 | 5.3 | 107.2 | 5.2 |

^a Derived from simultaneous fit of *TESS* photometry and RV measurements.

^b *TESS* 2 minute cadence data.

^c *TESS* 30 minute cadence data.

^d Impact parameter.

^e From 1st to last (4th) contacts.

^f From 2nd to 3rd contacts.

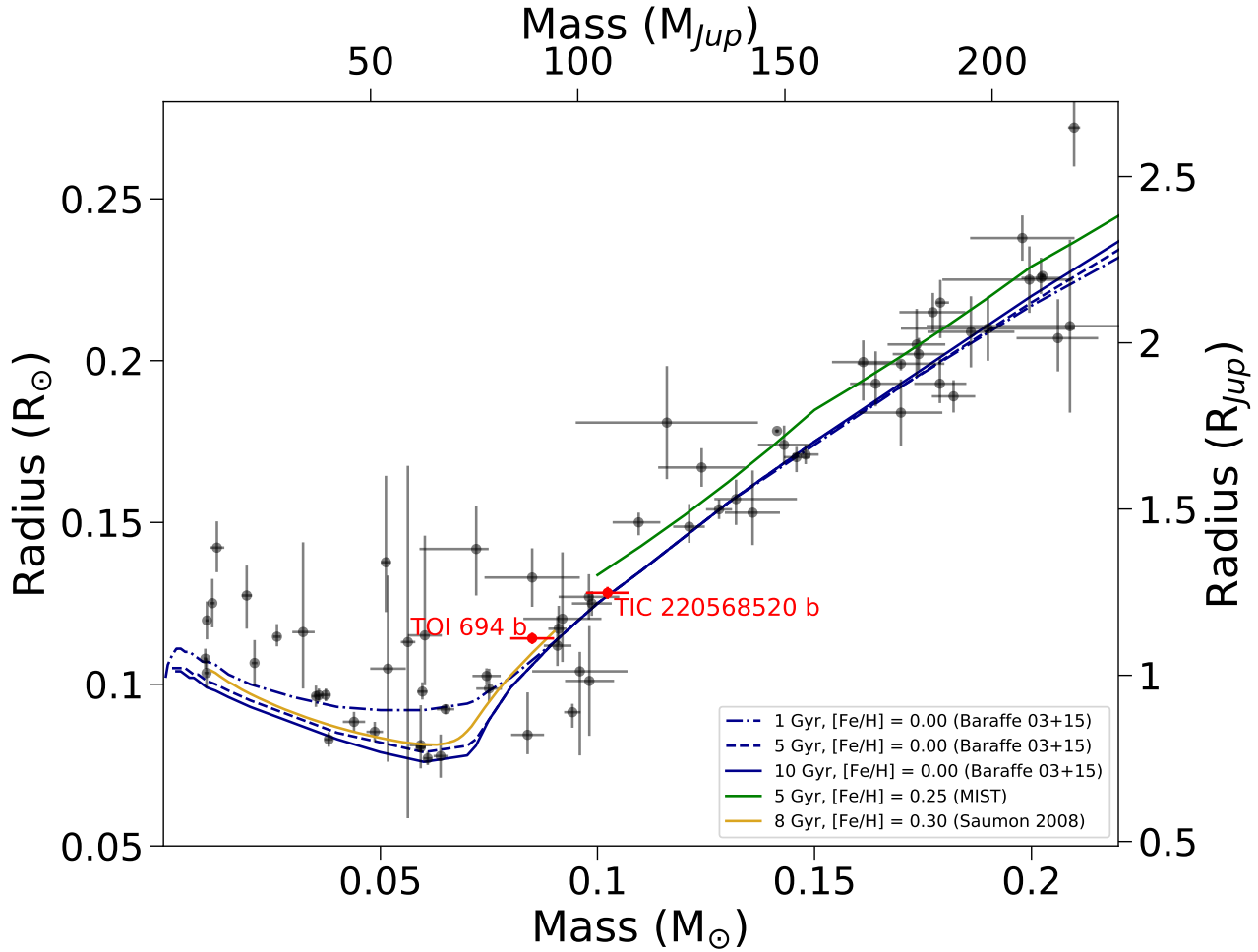


FIG. 10.— Radius-mass diagram for the massive planets, brown dwarfs, and low mass stars listed in Table 4. The blue lines are models for low mass stars and substellar objects with solar metallicity from Baraffe et al. (2015) and Baraffe et al. (2003). The green line is derived from MIST evolutionary tracks for $[\text{Fe}/\text{H}] = 0.25$. The gold line is a model from Saumon & Marley (2008) for $[\text{Fe}/\text{H}] = 0.3$. RIK 72 b is a $\sim 60 M_{\text{Jup}}$ transiting brown dwarf that is not shown due to its inflated radius of $3.10 R_{\text{Jup}}$ (David et al. 2019).

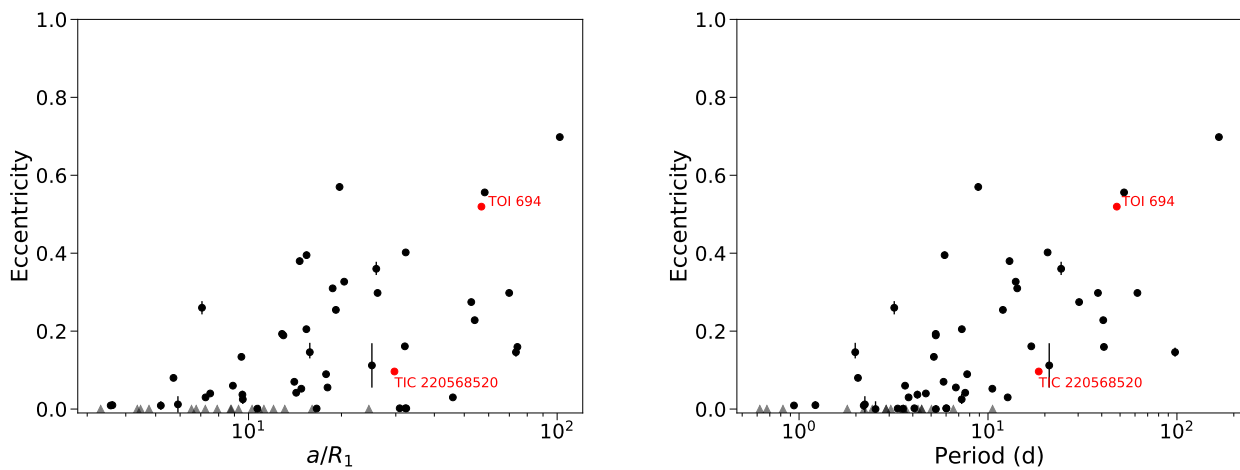


FIG. 11.— Eccentricity as a function of scaled semi-major axis (left) and period (right) for the substellar and stellar companions listed in Table 4. The scaled semi-major axis for each system is determined using Kepler’s Third Law. The two systems studied here are labeled and marked in red. Error bars are plotted for all systems, but for some they are smaller than the size of the marker. Faded triangles represent systems where the eccentricity was fixed to 0.

ted in the right panels of Figures 2 and 4, respectively. For each object we calculated the mean and standard deviation (root mean square) of all measurements determined to be within the secondary eclipse while removing 5- σ outliers. For TOI 694 the measured secondary eclipse depth of the binned 2-minute cadence data is -75 ± 1164 ppm, and for TIC 220568520 it is 190 ± 811 ppm. While these are obviously non-detections, they are consistent with the expected *TESS*-band shallow secondary eclipses given the expected effective temperatures of the small low-mass companions. By assuming blackbody spectra and integrating across the *TESS* band we derive an expected secondary eclipse depth of ≈ 300 ppm for TOI 694 assuming its effective temperature is 2,600 K, and ≈ 580 ppm for TIC 220568520 assuming its effective temperature is 2,800 K.

While the secondary eclipses are not detected in *TESS* data and are too shallow to be detected from the ground in visible light, they are expected to be deeper, and perhaps detectable, in longer wavelengths. For example, in the *K*-band (centered around $2.1 \mu\text{m}$) the expected depths are ≈ 2300 ppm and ≈ 3900 ppm, for TOI 694 and TIC 220568520, respectively. More broadly, a comparison between the expected secondary eclipse depths and the uncertainty of the measured secondary eclipse depths (see previous paragraph) shows that for similar objects but with shorter orbital periods (and hence longer eclipses in phase) and brighter primary stars the noise level can potentially allow a detection of the secondary eclipse for low-mass stars.

5. SUMMARY

We presented the discovery of two low-mass stars that are transiting (eclipsing) binary companions to Sun-like stars with eccentric orbits. The two low-mass stars are at the very bottom of the main sequence, close to and above the Hydrogen burning mass threshold. They join a short but growing list of low-mass stars with well-measured mass and radius. The relatively long orbital period of both systems means that the low-mass stars' radius is not likely to be impacted by enhanced magnetic fields, and we find their position in the radius-mass diagram to be consistent with theoretical models.

These discoveries emphasize the potential of transit surveys for detecting rare transiting low-mass binary companions, since given the similarity in radius of objects between ~ 1 Jupiter mass gas-giant planets through ~ 100 Jupiter mass stars, transiting gas-giant planet candidates are also, by definition, low-mass star candidates. During the *TESS* Extended Mission the two targets studied here will be observed again, leading to a refined transit light curve measurement and tighter upper limits on the secondary eclipse or possibly a secondary eclipse detection.

We acknowledge the use of *TESS* Alert data. These data are derived from pipelines at the *TESS* Science Office and at the *TESS* Science Processing Operations Center. Funding for the *TESS* mission is provided by NASA's Science Mission directorate. This paper includes data collected by the *TESS* mission, which are publicly available from the Mikulski Archive for Space Telescopes (MAST). Resources supporting this work were provided by the NASA High-End Computing (HEC) Program through the NASA Advanced Supercomputing (NAS) Division at Ames Research Center. This research has made use of the NASA Exoplanet Archive, which is operated by the California Institute of Technology, under contract with NASA under the Exoplanet Exploration Program. This work has been carried out within the framework of the National Centre of Competence in Research PlanetS supported by the Swiss National Science Foundation. MNG acknowledges support from MIT's Kavli Institute as a Torres postdoctoral fellow. LAdS is supported by funding from the European Research Council (ERC) under the European Unions Horizon 2020 research and innovation programme (project FOUR ACES; grant agreement No 724427). AJ acknowledges support from FONDECYT project 1171208 and by the Ministry for the Economy, Development, and Tourism's Programa Iniciativa Científica Milenio through grant IC120009, awarded to the Millennium Institute of Astrophysics (MAS).

Facilities: *TESS*, ANU:2.3m (Echelle), Euler 1.2m (CORALIE) MPG/ESO:2.2m (FEROS), SMARTS:1.5m (CHIRON), SOAR (HRCam)

REFERENCES

- Albrecht, S., Reffert, S., Snellen, I., et al. 2007, *A&A*, 474, 565 8
 Andersen, M., Meyer, M. R., Greissl, J., et al. 2008, *ApJ*, 683, L183 2
 Baraffe, I., Chabrier, G., Barman, T. S., et al. 2003, *A&A*, 402, 701 8, 10
 Baraffe, I., Homeier, D., Allard, F., et al. 2015, *A&A*, 577, A42 8, 10
 Bayliss, D., Hojjatpanah, S., Santerne, A., et al. 2017, *AJ*, 153, 15 14
 Beatty, T. G., Fernández, J. M., Latham, D. W., et al. 2007, *ApJ*, 663, 573 15
 Bonnell, I., Arcoragi, J.-P., Martel, H., et al. 1992, *ApJ*, 400, 579 8
 Bonnell, I. A. 1994, *MNRAS*, 269, 837 8
 Bonnell, I. A., Larson, R. B., & Zinnecker, H. 2007, *Protostars and Planets V*, 149 2
 Bonomo, A. S., Sozzetti, A., Santerne, A., et al. 2015, *A&A*, 575, A85 14
 Bouchy, F., Bonomo, A. S., Santerne, A., et al. 2011, *A&A*, 533, A83
 Bouchy, F., Deleuil, M., Guillot, T., et al. 2011, *A&A*, 525, A68 14
 Brahm, R., Jordán, A., & Espinoza, N. 2017, *PASP*, 129, 034002 4
 Brahm, R., Espinoza, N., Jordán, A., et al. 2019, *AJ*, 158, 45 4
 Buchhave, L. A., Latham, D. W., Johansen, A., et al. 2012, *Nature*, 486, 375 5
 Burrows, A., Heng, K., & Nampaisarn, T. 2011, *ApJ*, 736, 47 8
 Cañas, C. I., Bender, C. F., Mahadevan, S., et al. 2018, *ApJ*, 861, L4 14
 Carmichael, T. W., Latham, D. W., & Vanderburg, A. M. 2019, *AJ*, 158, 38 14
 Carmichael, T. W., Quinn, S. N., Mustill, A. J., et al. 2020, *arXiv e-prints*, arXiv:2002.01943 14
 Castelli, F., & Hubrig, S. 2004, *A&A*, 425, 263 2
 Chabrier, G. 2003, *PASP*, 115, 763 2
 Chabrier, G., Gallardo, J., & Baraffe, I. 2007, *A&A*, 472, L17 2, 8
 Chaturvedi, P., Chakraborty, A., Anandarao, B. G., et al. 2016, *MNRAS*, 462, 554 2, 14
 Choi, J., Dotter, A., Conroy, C., et al. 2016, *ApJ*, 823, 102
 Claret, A. 2017, *A&A*, 600, A30 7, 8

- Csizmadia, S., Hatzes, A., Gandolfi, D., et al. 2015, *A&A*, 584, A13 14
- Cutri, R. M., Skrutskie, M. F., van Dyk, S., et al. 2003, *VizieR Online Data Catalog*, II/246 5
- David, T. J., Hillenbrand, L. A., Gillen, E., et al. 2019, *ApJ*, 872, 161 8, 10, 14
- Deleuil, M., Deeg, H. J., Alonso, R., et al. 2008, *A&A*, 491, 889 14
- Díaz, R. F., Damiani, C., Deleuil, M., et al. 2013, *A&A*, 551, L9 14
- Díaz, R. F., Montagnier, G., Leconte, J., et al. 2014, *A&A*, 572, A109 2, 14
- Donati, J.-F., Semel, M., Carter, B. D., et al. 1997, *MNRAS*, 291, 658 2
- Dotter, A. 2016, *ApJS*, 222, 8 8
- Doyle, L. R., Carter, J. A., Fabrycky, D. C., et al. 2011, *Science*, 333, 1602 15
- Fabrycky, D., & Tremaine, S. 2007, *ApJ*, 669, 1298 8
- Fernandez, J. M., Latham, D. W., Torres, G., et al. 2009, *ApJ*, 701, 764 15
- Foreman-Mackey, D., Hogg, D. W., Lang, D., et al. 2013, *PASP*, 125, 306 7
- Foreman-Mackey, D., Agol, E., Ambikasaran, S., et al. 2017, *celerite: Scalable 1D Gaussian Processes in C++, Python, and Julia*, ascl:1709.008
- Gaia Collaboration, Brown, A. G. A., Vallenari, A., et al. 2018, *A&A*, 616, A1 5
- Gaudi, B. S., & Winn, J. N. 2007, *ApJ*, 655, 550 8
- Gill, S., Maxted, P. F. L., Evans, J. A., et al. 2019, *A&A*, 626, A119 15
- Gill, S., Bayliss, D., Cooke, B. F., et al. 2020, *MNRAS*, 491, 1548 15
- Gill, S., Cooke, B. F., Bayliss, D., et al. 2020, *arXiv e-prints*, arXiv:2002.09311 15
- Gillen, E., Hillenbrand, L. A., David, T. J., et al. 2017, *ApJ*, 849, 11 14, 15
- Gómez Maqueo Chew, Y., Morales, J. C., Faedi, F., et al. 2014, *A&A*, 572, A50 15
- Gould, A., Pepper, J., & DePoy, D. L. 2003, *ApJ*, 594, 533 2
- Günther, M. N., & Daylan, T. 2019, *allesfitter: Flexible star and exoplanet inference from photometry and radial velocity*, ascl:1903.003 7
- Günther, M. N., & Daylan, T. 2020, *arXiv e-prints*, arXiv:2003.14371 7
- Han, E., Muirhead, P. S., & Swift, J. J. 2019, *AJ*, 158, 111 8, 15
- Hebb, L., Wyse, R. F. G., Gilmore, G., et al. 2006, *AJ*, 131, 555 15
- Henden, A. A., Templeton, M., Terrell, D., et al. 2016, *VizieR Online Data Catalog*, II/336 5
- Hilditch, R. W. 2001, *An Introduction to Close Binary Stars* 8
- Hodžić, V., Triaud, A. H. M. J., et al. 2018, *MNRAS*, 481, 5091 14
- Hut, P. 1981, *A&A*, 99, 126 8
- Irwin, J., Buchhave, L., Berta, Z. K., et al. 2010, *ApJ*, 718, 1353 14
- Irwin, J. M., Charbonneau, D., Esquerdo, G. A., et al. 2018, *AJ*, 156, 140 14
- Jackman, J. A. G., Wheatley, P. J., Bayliss, D., et al. 2019, *MNRAS*, 2175 14
- Jenkins, J. M., Twicken, J. D., McCauliff, S., et al. 2016, *Proc. SPIE*, 99133E 2
- Jordán, A., Brahm, R., Espinoza, N., et al. 2020, *AJ*, 159, 145 4
- Kauffer, A., Stahl, O., Tubbesing, S., et al. 1999, *The Messenger*, 95, 8 4
- Kesseli, A. Y., Muirhead, P. S., Mann, A. W., et al. 2018, *AJ*, 155, 225 2, 8
- Kipping, D. M. 2013, *MNRAS*, 435, 2152 7
- Kraus, A. L., Douglas, S. T., Mann, A. W., et al. 2017, *ApJ*, 845, 72 15
- Kreidberg, L. 2015, *PASP*, 127, 1161
- Krumholz, M. R. 2014, *Phys. Rep.*, 539, 49 2
- Li, J., Tenenbaum, P., Twicken, J. D., et al. 2019, *PASP*, 131, 024506 8
- Lindgren, L., Hernández, J., Bombrun, A., et al. 2018, *A&A*, 616, A2 6
- Mamajek, E. E., & Hillenbrand, L. A. 2008, *ApJ*, 687, 1264 7
- Marsh, T. R. 1989, *PASP*, 101, 1032 4
- Maxted, P. F. L. 2016, *A&A*, 591, A111 7
- Mazeh, T. 2008, *EAS Publications Series*, 1 2, 8
- Montet, B. T., Johnson, J. A., Muirhead, P. S., et al. 2015, *ApJ*, 800, 134 14
- Morton, T. D. 2015, *isochrones: Stellar model grid package*, ascl:1503.010 5
- Moutou, C., Bonomo, A. S., Bruno, G., et al. 2013, *A&A*, 558, L6 14
- Nefs, S. V., Birkby, J. L., Snellen, I. A. G., et al. 2013, *MNRAS*, 431, 3240 15
- Nowak, G., Palle, E., Gandolfi, D., et al. 2017, *AJ*, 153, 131 14
- Nutzman, P., & Charbonneau, D. 2008, *PASP*, 120, 317 2
- Ofir, A., Gandolfi, D., Buchhave, L., et al. 2012, *MNRAS*, 423, L1 15
- Parviainen, H., Gandolfi, D., Deleuil, M., et al. 2014, *A&A*, 562, A140 14
- Paxton, B., Bildsten, L., Dotter, A., et al. 2011, *ApJS*, 192, 3 8
- Paxton, B., Cantiello, M., Arras, P., et al. 2013, *ApJS*, 208, 4
- Paxton, B., Marchant, P., Schwab, J., et al. 2015, *ApJS*, 220, 15
- Pepe, F., Mayor, M., Rupprecht, G., et al. 2002, *The Messenger*, 110, 9 4
- Persson, C. M., Csizmadia, S., Mustill, A. J., et al. 2019, *A&A*, 628, A64 14
- Pont, F., Bouchy, F., Melo, C., et al. 2005, *A&A*, 438, 1123 2, 15
- Pont, F., Melo, C. H. F., Bouchy, F., et al. 2005, *A&A*, 433, L21 14
- Pont, F., Moutou, C., Bouchy, F., et al. 2006, *A&A*, 447, 1035 14
- Pringle, J. E. 1989, *MNRAS*, 239, 361 8
- Queloz, D., Mayor, M., Udry, S., et al. 2001, *The Messenger*, 105, 1 3
- Ribas, I. 2006, *Ap&SS*, 304, 89 2, 8
- Ricker, G. R., Winn, J. N., Vanderspek, R., et al. 2015, *Journal of Astronomical Telescopes, Instruments, and Systems*, 1, 014003
- Saunon, D., & Marley, M. S. 2008, *ApJ*, 689, 1327 8, 10
- Schlegel, D. J., Finkbeiner, D. P., & Davis, M. 1998, *ApJ*, 500, 525 7
- Shporer, A., Zhou, G., Vanderburg, A., et al. 2017, *ApJ*, 847, L18 14, 15
- Siverd, R. J., Beatty, T. G., Pepper, J., et al. 2012, *ApJ*, 761, 123 14
- Smith, J. C., Stumpe, M. C., Van Cleve, J. E., et al. 2012, *PASP*, 124, 1000 2
- Southworth, J., Hinse, T. C., Dominik, M., et al. 2009, *ApJ*, 707, 167 14
- Speagle, J. S. 2019, *arXiv e-prints*, arXiv:1904.02180
- Stassun, K. G., Collins, K. A., & Gaudi, B. S. 2017, *AJ*, 153, 136 6
- Stassun, K. G., Corsaro, E., Pepper, J. A., et al. 2018, *AJ*, 155, 22 6
- Stassun, K. G., Oelkers, R. J., Pepper, J., et al. 2018, *AJ*, 156, 102 4, 5
- Stassun, K. G., & Torres, G. 2016, *AJ*, 152, 180 6
- Stassun, K. G., & Torres, G. 2018, *ApJ*, 862, 61 7
- Stumpe, M. C., Smith, J. C., Van Cleve, J. E., et al. 2012, *PASP*, 124, 985 2
- Stumpe, M. C., Smith, J. C., Catanzarite, J. H., et al. 2014, *PASP*, 126, 100 2
- Šubjak, J., Sharma, R., Carmichael, T. W., et al. 2019, *arXiv e-prints*, arXiv:1909.07984 14
- Tal-Or, L., Mazeh, T., Alonso, R., et al. 2013, *A&A*, 553, A30 14
- Tokovinin, A., Fischer, D. A., Bonati, M., et al. 2013, *PASP*, 125, 1336 2
- Tokovinin, A. 2018, *PASP*, 130, 035002 4
- Torres, G., Andersen, J., & Giménez, A. 2010, *A&A Rev.*, 18, 67 2, 7, 8
- Triaud, A. H. M. J. 2018, *Handbook of Exoplanets*, 2 8
- Triaud, A. H. M. J., Hebb, L., Anderson, D. R., et al. 2013, *A&A*, 549, A18 14
- von Boetticher, A., Triaud, A. H. M. J., Queloz, D., et al. 2019, *A&A*, 625, A150 2, 8, 14, 15
- Winn, J. N., Holman, M. J., Torres, G., et al. 2008, *ApJ*, 683, 1076 14
- Zhou, G., Bayliss, D., Hartman, J. D., et al. 2014, *MNRAS*, 437, 2831 14, 15
- Zhou, G., Bayliss, D., Penev, K., et al. 2014, *AJ*, 147, 144 2, 3
- Zhou, G., Bayliss, D., Hartman, J. D., et al. 2015, *MNRAS*, 451, 2263 15

Zhou, G., Bakos, G. Á., Bayliss, D., et al. 2019, *AJ*, 157, 31–14
Ziegler, C., Tokovinin, A., Briceño, C., et al. 2020, *AJ*, 159, 19–5
Zimmerman, M. K., Thompson, S. E., Mullally, F., et al. 2017,
ApJ, 846, 147–8

TABLE 4
CATALOG OF LOW MASS COMPANIONS WITH MEASURED MASSES AND RADII

| System | M_2 (M_J) | σ_{M_2} (M_J) | R_2 (R_J) | σ_{R_2} (R_J) | P (days) | e | σ_e | M_1 (M_\odot) | σ_{M_1} (M_\odot) | R_1 (R_\odot) | σ_{R_1} (R_\odot) | T_{eff} (K) | $\sigma_{T_{eff}}$ (K) | Reference |
|----------------|--------------------|-----------------------------|--------------------|-----------------------------|---------------|----------------|----------------------|------------------------|---------------------------------|------------------------|---------------------------------|------------------|---------------------------|----------------------------|
| Kepler-75 | 10.1 | 0.4 | 1.05 | 0.03 | 8.88 | 0.57 | 0.01 | 0.91 | 0.04 | 0.89 | 0.02 | 5200 | 100 | Bonomo et al. 2015 |
| CoRoT-27 | 10.4 | 0.6 | 1.01 | 0.04 | 3.57 | 0 ^a | - | 1.05 | 0.11 | 1.08 | +0.16 -0.08 | 5900 | 120 | Parviainen et al. 2014 |
| WASP-18 | 10.52 | 0.38 | 1.165 | 0.057 | 0.94 | 0.0092 | 0.0028 | 1.281 | 0.069 | 1.230 | 0.047 | 6400 | 100 | Southworth et al. 2009 |
| XO-3 | 11.8 | 0.6 | 1.22 | 0.07 | 3.19 | 0.260 | 0.017 | 1.21 | 0.07 | 1.38 | 0.08 | 6429 | 100 | Winn et al. 2008 |
| HATS 70 | 12.9 | +1.8 -1.6 | 1.384 | +0.079 -0.074 | 1.888 | < 0.18 | - | 1.78 | 0.12 | 1.881 | +0.059 -0.066 | 7930 | +630 -820 | Zhou et al. 2019 |
| Kepler-39 | 20.1 | +1.3 -1.2 | 1.24 | +0.09 -0.10 | 21.09 | 0.112 | 0.057 | 1.29 | +0.06 -0.07 | 1.40 | 0.10 | 6350 | 100 | Bonomo et al. 2015 |
| CoRoT-3 | 22.0 | 0.7 | 1.037 | 0.069 | 4.26 | 0 ^a | - | 1.37 | 0.09 | 1.56 | 0.09 | 6740 | 140 | Deleuil et al. 2008 |
| KELT-1 | 27.38 | 0.93 | 1.116 | +0.038 -0.029 | 1.22 | 0.01 | +0.010 -0.007 | 1.335 | 0.063 | 1.471 | +0.045 -0.035 | 6516 | 49 | Siverv et al. 2012 |
| NLTT 41135 | 33.7 | +2.8 -2.6 | 1.13 | +0.27 -0.17 | 2.889 | 0 ^a | - | 0.188 | +0.026 -0.022 | 0.21 | +0.016 -0.014 | 3230 | 130 | Irwin et al. 2010 |
| EPIC 219388192 | 36.8 | 1.0 | 0.937 | 0.032 | 5.29 | 0.1929 | 0.0019 | 1.01 | 0.04 | 1.01 | 0.03 | 5850 | 50 | Nowak et al. 2017 |
| WASP-128 | 37.5 | 0.8 | 0.94 | 0.02 | 2.21 | 0 ^a | - | 1.16 | 0.04 | 1.16 | 0.02 | 5950 | 85 | Hodžić et al. 2018 |
| CWW 89 A | 39.21 | 1.10 | 0.941 | 0.019 | 5.293 | 0.1891 | 0.0022 | 1.101 | +0.039 -0.045 | 1.029 | 0.016 | 5755 | 49 | Carmichael et al. 2019 |
| KOI 205 | 39.9 | 1.0 | 0.807 | 0.022 | 11.72 | < 0.031 | - | 0.925 | 0.033 | 0.841 | 0.020 | 5237 | 60 | Díaz et al. 2013 |
| TOI 1406 | 46.0 | 2.7 | 0.86 | 0.03 | 10.57415 | 0 ^a | - | 1.18 | 0.09 | 1.35 | 0.03 | 6290 | 100 | Carmichael et al. 2020 |
| EPIC 212036875 | 51 | 2 | 0.83 | 0.03 | 5.17 | 0.134 | 0.002 | 1.15 | 0.08 | 1.41 | 0.05 | 6230 | 90 | Persson et al. 2019 |
| TOI-503 | 53.7 | 1.2 | 1.34 | +0.26 -0.15 | 3.677 | 0 ^a | - | 1.80 | 0.06 | 1.70 | 0.05 | 7650 | 160 | Šubjak et al. 2019 |
| AD 3116 | 54.2 | 4.3 | 1.02 | 0.28 | 1.983 | 0.146 | +0.024 -0.016 | 0.276 | 0.020 | 0.29 | 0.08 | 3184 | 29 | Gillen et al. 2017 |
| CoRoT-33 | 59 | +1.8 -1.7 | 1.1 | 0.53 | 5.819 | 0.07 | 0.0016 | 0.86 | 0.04 | 0.94 | +0.14 -0.08 | 5225 | 80 | Csizmádia et al. 2015 |
| RIK 72 | 59.2 | 6.8 | 3.10 | 0.31 | 97.76 | 0.146 | 0.0116 | 0.439 | 0.044 | 0.961 | 0.096 | 3349 | 142 | David et al. 2019 |
| LHS 6343 C | 62.1 | 1.2 | 0.783 | 0.011 | 12.713 | 0.03 | 0.002 | 0.358 | 0.011 | 0.373 | 0.005 | 3431 | 21 | Montet et al. 2015 |
| KOI 415 | 62.1 | 2.7 | 0.790 | +0.120 -0.070 | 166.8 | 0.698 | 0.002 | 0.94 | 0.06 | 1.250 | +0.015 -0.010 | 5810 | 80 | Moutou et al. 2013 |
| WASP-30 | 62.50 | 1.20 | 0.951 | +0.028 -0.024 | 4.16 | < 0.0044 | - | 1.249 | +0.032 -0.036 | 1.389 | +0.033 -0.025 | 6202 | +42 -51 | Triaud et al. 2013 |
| CoRoT-15 | 63.1 | 4.1 | 1.12 | +0.30 -0.15 | 3.06 | 0 ^a | - | 1.32 | 0.12 | 1.46 | +0.31 -0.14 | 6350 | 200 | Bouchy et al. 2011b |
| TOI 569 | 63.8 | 1.0 | 0.75 | 0.02 | 6.55604 | 0 ^a | - | 1.21 | 0.03 | 1.48 | 0.03 | 5705 | 76 | Carmichael et al. 2020 |
| EPIC 201702477 | 66.9 | 1.7 | 0.757 | 0.065 | 40.74 | 0.2281 | 0.0026 | 0.870 | 0.031 | 0.901 | 0.057 | 5571 | 70 | Bayliss et al. 2017 |
| LP 261-75 | 68.1 | 2.1 | 0.898 | 0.015 | 1.882 | < 0.007 | - | 0.300 | 0.015 | 0.313 | 0.005 | 3100 | 50 | Irwin et al. 2018 |
| NGTS-7A | 75.5 | +3 -13.7 | 1.38 | +0.13 -0.14 | 0.676 | 0 ^a | - | 0.480 | 0.075 | 0.61 | 0.06 | 3359 | +106 -89 | Jackman et al. 2019 |
| KOI 189 | 78.0 | 3.4 | 0.998 | 0.023 | 30.36 | 0.2746 | 0.0037 | 0.764 | 0.051 | 0.733 | 0.017 | 4952 | 40 | Díaz et al. 2014 |
| Kepler-503 | 78.6 | 3.1 | 0.96 | +0.06 -0.04 | 7.258 | 0.025 | +0.014 -0.012 | 1.154 | +0.047 -0.042 | 1.764 | +0.08 -0.068 | 5690 | +100 -110 | Cañas et al. 2018 |
| EBLM J0555-57 | 87.90 | 3.98 | 0.821 | +0.128 -0.058 | 7.758 | 0.0895 | +0.0035 -0.0036 | 1.180 | +0.082 -0.079 | 1.00 | +0.14 -0.07 | 6386 | 124 | von Boetticher et al. 2019 |
| OGLE-TR-123 | 89.0 | 11.5 | 1.294 | 0.088 | 1.8 | 0 ^a | - | 1.29 | 0.26 | 1.55 | 0.1 | 6700 | 300 | Pont et al. 2006 |
| TOI 694 | 89.8 | 5.3 | 1.11 | 0.02 | 48.05125 | 0.5212 | 0.0021 | 0.967 | +0.047 -0.04 | 0.998 | +0.010 -0.012 | 5496 | +87 -81 | This work |
| KOI-607 | 95.1 | +3.4 -3.3 | 1.089 | +0.089 -0.061 | 5.894 | 0.395 | +0.0091 -0.0090 | 0.993 | +0.050 -0.052 | 0.915 | +0.031 -0.028 | 5418 | +87 -85 | Carmichael et al. 2019 |
| J1219-39 | 95.4 | +1.9 -2.5 | 1.140 | +0.069 -0.049 | 6.76 | 0.05539 | +0.00023 -0.00022 | 0.826 | +0.032 -0.029 | 0.811 | +0.038 -0.024 | 5412 | +81 -65 | Triaud et al. 2013 |
| OGLE-TR-122 | 96.3 | 9.4 | 1.17 | +0.20 -0.15 | 7.27 | 0.205 | 0.008 | 0.98 | 0.14 | 1.05 | +0.20 -0.09 | 5700 | 300 | Pont et al. 2005a |
| K2-76 | 98.7 | 2.0 | 0.889 | +0.025 -0.047 | 11.99 | 0.2545 | +0.0070 -0.0065 | 0.964 | 0.026 | 1.171 | +0.033 -0.060 | 5747 | +64 -70 | Shporer et al. 2017 |
| C101186644 | 101 | 12 | 1.01 | +0.25 | 20.68 | 0.402 | - | 1.2 | 0.2 | 1.07 | 0.07 | 6090 | 200 | Tal-Or et al. 2013 |
| J2343+29 | 103 | 7 | 1.236 | 0.068 | 16.95 | 0.161 | +0.0015 -0.0027 | 0.864 | +0.097 -0.080 | 0.854 | +0.050 -0.060 | 5150 | +90 -60 | Chaturvedi et al. 2016 |
| EBLM J0954-23 | 102.8 | +6.0 -5.9 | 0.983 | 0.165 | 7.575 | 0.04186 | +0.00094 -0.00092 | 1.166 | +0.080 -0.082 | 1.23 | 0.17 | 6406 | 124 | von Boetticher et al. 2019 |
| KOI 686 | 103 | 5 | 1.22 | 0.04 | 52.51 | 0.556 | 0.0037 | 0.983 | 0.074 | 1.04 | 0.03 | 5750 | 120 | Díaz et al. 2014 |
| TIC 220568520 | 107.8 | 5.2 | 1.248 | 0.018 | 18.55741 | 0.0956 | +0.0032 -0.0030 | 1.030 | +0.043 -0.042 | 1.007 | +0.010 -0.009 | 5589 | 81 | This work |
| HATS 550-016 | 115 | +5 -6 | 1.46 | +0.03 -0.04 | 2.05 | 0.08 | -1 | 0.97 | +0.05 -0.06 | 1.22 | +0.02 -0.03 | 6420 | 90 | Zhou et al. 2014 |

TABLE 4
(CONTINUED)

| System | M_2 (M_J) | σ_{M_2} (M_J) | R_2 (R_J) | σ_{R_2} (R_J) | P (days) | e | σ_e | M_1 (M_\odot) | σ_{M_1} (M_\odot) | R_1 (R_\odot) | σ_{R_1} (R_\odot) | T_{eff} (K) | $\sigma_{T_{eff}}$ (K) | Reference |
|---------------------|--------------------|-----------------------------|--------------------|-----------------------------|---------------|----------------|----------------------|------------------------|---------------------------------|------------------------|---------------------------------|------------------|---------------------------|-------------------------------|
| OGLE-TR-106 | 121 | 22 | 1.76 | 0.17 | 2.54 | 0 | 0.02 | - | - | 1.31 | 0.09 | - | - | Pont et al. 2005b |
| EBLM J1431-11 | 126.9 | +3.77 -3.87 | 1.447 | +0.0681 -0.0487 | 4.45 | 0 ^a | - | 1.200 | +0.056 -0.055 | 1.114 | +0.043 -0.028 | 6161 | 124 | von Boetticher et al. 2019 |
| HAT-TR-205-013 | 130 | 11 | 1.63 | 0.06 | 2.23 | 0.012 | 0.021 | 1.04 | 0.13 | 1.28 | 0.04 | 6295 | - | Beatty et al. 2007 |
| TIC 231005575 | 134.1 | 3.1 | 1.499 | 0.029 | 61.777 | 0.298 | +0.004 -0.001 | 1.045 | 0.035 | 0.992 | 0.050 | 5500 | 85 | Gill et al. 2020a |
| HATS 551-021 | 138 | +15 -5 | 1.53 | +0.06 -0.08 | 3.64 | 0.06 | - | 1.10 | 0.10 | 1.20 | +0.08 -0.01 | 6670 | 220 | Zhou et al. 2014 |
| EBLM J2017+02 | 142.2 | +6.6 -6.7 | 1.489 | +0.127 -0.097 | 0.822 | 0 ^a | - | 1.105 | +0.074 -0.072 | 1.196 | +0.080 -0.050 | 6161 | 124 | von Boetticher et al. 2019 |
| KIC 1571511 | 148.0 | 0.5 | 1.735 | +0.005 -0.006 | 14.02 | 0.3269 | 0.0027 | 1.265 | +0.036 -0.030 | 1.343 | +0.012 -0.010 | 6195 | 50 | Ofr et al. 2012 |
| WTS 19g-4-02069 | 150 | 6 | 1.69 | 0.06 | 2.44 | 0 ^a | - | 0.53 | 0.02 | 0.51 | 0.01 | 3300 | 140 | Nefs et al. 2013 |
| K2-51 | 152.8 | +3.4 -3.0 | 1.656 | +0.031 -0.045 | 13.001 | 0.3797 | +0.0090 -0.0058 | 1.068 | +0.032 -0.029 | 1.695 | +0.037 -0.049 | 5908 | +63 -64 | Shporer et al. 2017 |
| TIC 238855958 | 155.0 | 3.1 | 1.664 | 0.029 | 38.195 | 0.298 | - | 1.514 | 0.037 | 2.159 | 0.037 | 6280 | 85 | Gill et al. 2020b |
| K2-67 | 168.9 | +7.0 -7.5 | 1.942 | +0.065 -0.116 | 24.388 | 0.36 | +0.018 -0.016 | 0.916 | +0.290 -0.031 | 1.399 | +0.056 -0.029 | 5579 | +78 -77 | Shporer et al. 2017 |
| EBLM J0543-56 | 171.9 | +6.0 -6.2 | 1.877 | +0.067 -0.068 | 4.464 | 0 ^a | - | 1.276 | +0.072 -0.070 | 1.255 | +0.054 -0.036 | 6223 | 124 | von Boetticher et al. 2019 |
| HATS 551-019 | 178 | 10 | 1.79 | 0.10 | 4.69 | 0.04 | - | 1.10 | +0.05 -0.09 | 1.70 | 0.09 | 6380 | 170 | Zhou et al. 2014 |
| KIC 7605600 | 178 | 11 | 1.94 | +0.01 -0.02 | 3.326 | 0.0013 | +0.0043 -0.0008 | 0.53 | 0.02 | 0.501 | +0.001 -0.002 | - | - | Han et al. 2019 |
| EBLM J1038-37 | 181.8 | +6.9 -7.0 | 1.995 | +0.107 -0.097 | 5.022 | 0 ^a | - | 1.176 | +0.072 -0.070 | 1.132 | +0.052 -0.048 | 5885 | 124 | von Boetticher et al. 2019 |
| EBLM J2349-32 | 182.3 | 6.3 | 1.966 | 0.049 | 3.5496972 | 0.001 | 0.002 | 0.991 | 0.049 | 0.965 | 0.022 | 6130 | 85 | Gill et al. 2019 |
| EBLM J1013+01 | 185.7 | +7.9 -8.1 | 2.092 | 0.058 | 2.892 | 0 ^a | - | 1.036 | +0.070 -0.072 | 1.036 | +0.027 -0.026 | 5579 | 124 | von Boetticher et al. 2019 |
| EBLM J1115-36 | 187.4 | +6.4 -6.2 | 1.877 | +0.078 -0.088 | 10.543 | 0.0522 | +0.0038 -0.0037 | 1.369 | 0.072 | 1.579 | +0.048 -0.041 | 6605 | 124 | von Boetticher et al. 2019 |
| HATS 551-027 | 187.5 | +7.1 -1.0 | 2.121 | +0.107 -0.107 | 4.077 | 0.002 | - | 0.244 | 0.003 | 0.261 | +0.006 -0.009 | 3190 | 100 | Zhou et al. 2015 |
| EBLM J2308-46 | 190.7 | 5.2 | 1.839 | 0.049 | 2.199187 | 0.009 | 0.011 | 1.223 | 0.049 | 1.534 | 0.041 | 6185 | 85 | Gill et al. 2019 |
| J0113+31 | 194.9 | 10.5 | 2.033 | 0.107 | 14.28 | 0.3098 | 0.0005 | 0.945 | 0.045 | 1.378 | 0.058 | 5961 | 54 | Gómez Maqueo Chew et al. 2014 |
| 2MASS J0446+19 | 199 | 21 | 2.04 | 0.10 | 0.62 | 0 ^a | - | 0.47 | 0.05 | 0.56 | 0.02 | 3320 | 150 | Hebb et al. 2006 |
| T-Lyr-101662 | 207 | 13 | 2.32 | 0.07 | 4.23 | 0.037 | 0.01 | 0.77 | 0.08 | 1.14 | 0.03 | 6200 | 30 | Fernandez et al. 2009 |
| HATS 553-001 | 209 | +11 -21 | 2.19 | 0.10 | 3.8 | 0.03 | - | 1.20 | 0.10 | 1.58 | +0.08 -0.03 | 6230 | 250 | Zhou et al. 2014 |
| AD 3814 | 211.8 | 4.7 | 2.195 | +0.061 -0.048 | 6.02 | 0.00194 | +0.00253 -0.00057 | 0.3813 | 0.0074 | 0.3610 | 0.0033 | 3211 | +54 -36 | Gillen et al. 2017 |
| Kepler-16 | 212.2 | 0.7 | 2.201 | 0.006 | 41.08 | 0.15944 | +0.00662 -0.00061 | 0.6897 | +0.0035 -0.0034 | 0.6489 | 0.0013 | 4450 | 150 | Doyle et al. 2011 |
| EBLM J0339+03 | 215.9 | +9.7 -10.0 | 2.014 | +0.117 -0.100 | 3.581 | 0 ^a | - | 1.036 | +0.034 -0.076 | 1.210 | +0.055 -0.052 | 6132 | 124 | von Boetticher et al. 2019 |
| OGLE-TR-125 | 219 | 35 | 2.05 | 0.26 | 5.3 | 0 | 0.01 | - | - | 1.94 | 0.18 | - | - | Pont et al. 2005b |
| PTFEB132.707+19.810 | 219.8 | 1.5 | 2.647 | 0.117 | 6.016 | 0.0017 | 0.0006 | 0.3953 | 0.0020 | 0.363 | 0.008 | 3260 | 67 | Kraus et al. 2017 |

^a Eccentricity fixed at 0